The effect of the Region 2 currents location on the strength of the auroral electrojet and global distribution of ionospheric currents

S. Lyatskaya[1,3], N. Buzulukova[2,3]

[1] Catholic University of America

[2] University of Maryland, College Park

[3] NASA Goddard Space Flight Center

Corresponding author: Sonya Lyatskaya (lyatskys@cua.edu)

Key Points:

- Strong R2 currents provide robust closure for the ionospheric currents flowing from R1 system via auroral zone ionosphere.
- MLT distribution and strength of the auroral electrojet is sensitive to the R2 currents, with weaker and broader electrojet for more equatorial R2 location.
- Simulations show close characteristics to the observed events but also suggest to consider additional factors including substorm current wedge and auroral potential drop.

Abstract

In this study, we use a parametrized model of ionospheric electrodynamics to investigate the effect of Region 2 currents' location on the development and dynamics of the auroral electrojet (AE), using real cases data as input parameters for our simulations. We calculated the maps of equivalent ionospheric currents reproducing the events of interest, analyzed the results and compared with SuperMAG observations. The simulations have shown that strong R2 currents provide a robust closure for the ionospheric currents flowing from R1 via auroral zone ionosphere. We found that the highest magnitude westward auroral electrojet is in the day-to-dawn sector, while the equivalent ionospheric currents on the night-side have much lower magnitude. We suggest that the location of the R2 currents affects the entire distribution of ionospheric currents, changing the MLT location and magnitude of the maximum auroral electrojet. As the distance between the location of the maxima for the R1 and R2 current systems increases, the magnitude of the ionospheric currents decreases because the ionospheric currents spread over larger regions at low latitudes. When R2 currents cannot provide the proper closure, the ionospheric currents flow from the dawn to dusk over the night-side ionosphere, leading to the westward auroral electrojet development in the night region of the auroral zone. We analyzed features and magnitude of these currents and compared with observations.

Plain Language Summary

Solar wind is a stream of charged particles flowing from the Sun in all directions. When they reach planets with magnetic fields, like our Earth, they interact with these magnetic fields creating magnetosphere, which is similar to a magnetic bubble around the planet. Due to the interaction between the solar wind particles and Earth’s magnetic field, a giant loop of current is

formed in space that circulates between the solar wind, the magnetosphere and the Earth's ionosphere. These currents could sometimes cause the most spectacular phenomenon, Aurora Borealis in the Northern hemisphere, and Aurora Australis in the Southern. These auroras have distinctive ring-shaped structures that form around the polar caps. These formations are called auroral ovals or auroral zones. The auroras occur in the same place where the most intense currents flow, therefore it is important to understand the interactions between current systems and their ionospheric closures. The Region 1 currents appear at the inner (high geomagnetic latitudes) boundary of the auroral oval, and Region 2 currents appear at the outer (low geomagnetic latitudes) boundary of this oval. The interactions between these Region 1 and 2 currents occurs via highly conductive auroral oval, where observations of ionospheric currents provide information about the currents closure. Using numerical simulations and comparison with the observations, we studied how the location of R2 currents affects the development and dynamics of the ionospheric currents during geomagnetic disturbances, including geomagnetic substorms.

1. Introduction

The global three-dimensional magnetosphere-ionosphere current system is one of the most important phenomena in the Earth's environment. The interaction of the solar wind and the Earth magnetosphere can generate a number of geomagnetic phenomena, e.g. reconnection of the Earth's and interplanetary magnetic field (IMF) and hence convection of magnetic field lines, ionospheric and field aligned currents (FACs), etc.

The magnitude of currents depends on many conditions, for example, IMF direction, currents location, ionospheric conductivity, and a few others. Some of the conditions are relatively stable, such as ionospheric conductivity due to solar illumination, for example the sunlit regions of the ionosphere have higher conductivity due to ionization by the solar light. This condition changes relatively slowly with the movement of the Earth around the Sun.

Some other conditions may experience rapid changes, such as the ionospheric conductivity associated with auroral precipitation, the expansion and contraction of the polar cap, and the boundaries of the auroral zone [e.g., Akasofu, 1964].

These rapidly changing conditions are usually related to the orientation of the IMF, for example, the southward oriented IMF can reconnect with the Earth's magnetic field. This process results in significant penetration of the solar wind into the magnetosphere, causing auroras, polar caps expansion, equatorward shifting and expanding of the auroral zones, and strong field-aligned and ionospheric currents. The Region 1 (R1) FACs, which emerge at the polar cap boundaries, also develop at the lower latitude. The secondary FAC system, so called Region 2 (R2) currents, is generated at the equatorward boundaries of the auroral zone, which correspond to the plasma sheet inner boundary; these boundaries are also expanding and drifting equatorward. These current systems have been extensively studied and described in various articles [Iijima and Potemra, 1976; Weimer, 2001; Papitashvili et al., 2002; Anderson et al., 2005, Lyatsky et al., 1974, Ganushkina et al., 2018 and references therein].

Over the past decade, there have been significant advances in understanding the configuration, dynamics, and drivers for various current systems of the Earth's magnetosphere (e.g., review of current systems by Ganushkina et al., 2018 and references therein). The DMSP, SWARM, Iridium, AMPERE, MMS and CLUSTER missions allow detailed analysis of the

84 complex structure of currents, including the Region 2 currents. Ohtani et al., 2010 used DMSP
85 data to identify R1/R2 current systems and relate their boundaries to various precipitation
86 boundaries. It has been showed that the maximum energy flux for ion precipitation (b2i
87 boundary) is located inside R2 currents, and hence can be used as an identifier for R2 current.
88 Korth et al., 2014 have studied R1/R2 currents with Iridium data in order to correlate R1/R2
89 currents with auroral emissions obtained from TIMED data and found that the results are in
90 agreement with Ohtani et al., 2010. During geomagnetically active times, nightside R2 system
91 evolves as a response to substorm activity and modified by superposition with substorm current
92 wedge (Murphy et al., 2013). Since substorms ultimately brings plasma from the tail to the ring
93 current region, substorm current wedge can be viewed as an important link connecting R1/R2
94 systems during substorms (Kepko et al., 2015). An important interplay between global R1/R2
95 systems is established in Anderson et al., 2018. It has been found that R1 system do not fully
96 develop without R2 currents; they intensify together first at dayside, and then at nightside after
97 the onset of activity.
98 R2 currents have been successfully modelled over the past two decades using so-called ring
99 current models (Zheng et al., 2006 and references therein). A ring current model calculates
100 plasma distribution in the inner magnetosphere and compute R2 currents from Vasyliunas
101 equation (Toffoletto et al., 2003, equation 12). This approach produces large scale R2 currents,
102 both upward and downward (Zheng et al., 2006). If interchange instability occurs in the inner
103 magnetosphere, the model R2 system develops a characteristic pattern consisting of intermittent
104 upward/downward currents (Sazykin et al., 2002; Buzulukova et al., 2008).
105

Recent simulations with global MHD model coupled with the ring current module also demonstrate intermittent structure of R2 currents at nightside, resulting from the interaction of magnetotail bursty flows with dipole-like inner magnetosphere (Yu et al., 2017).

In this paper, we investigate the role of R2 current system using a parametrized model of ionospheric electrodynamics, where the location of R1 and R2 current systems is a parameter, as well as the magnitude of the currents, polar boundary electric field potential and ionospheric conductivity. This simplified approach is different from the sophisticated first-principles models mentioned above. Being less computationally expensive, it nevertheless makes it possible to disentangle important physical properties of magnetospheric current systems, often hidden in the self-consistent solution.

2. Model Input and Simulation Results

In current work, we have used the previously developed model of ionospheric electrodynamics (Lyatskaya et al., 2014, 2015, 2016), hereinafter L-2015, to analyze the impact of the R2 currents location on the global magnetosphere-ionospheric current system. The model uses as an input the location and magnitude of R1, R2 field-aligned currents, the ionospheric conductivity and the polar boundary electric field potential. The model produces ionospheric currents and field-aligned currents, including interhemispheric currents flowing between the northern and southern conjugate ionospheres in the case of asymmetry of ionospheric conductivities in two hemispheres. The model described in detail in Lyatskaya et al., 2015. For the simulation, we selected the season, when the impact of interhemispheric currents would be minimal.

One of the assumptions of the model is that the potential drop along magnetic field line in the auroral region is negligible. While this assumption is not always valid, it mimics a similar assumption adopted in global MHD codes with a separate module for ionospheric electrodynamics. While we anticipate the importance of auroral potential drop, we assume that it will not change the studied effects of R2 location quantitatively. The role of auroral potential drop will be investigated in another study.

As input to the model, we used an electric potential distribution at the boundaries of the auroral zone as boundary conditions of the simulation. The potential distribution at the polar cap was taken from the Active Magnetosphere and Planetary Electrodynamics Response Experiment (AMPERE) data products [Anderson, et al. 2008a, 2014, and references therein]. AMPERE data of the field aligned currents were used for both control purposes and as a means of defining the location of the R1 and R2 currents. We adopted Hardy et al. [1987] [see also Weimer, 1999] model for ionospheric conductivity for Kp=4 and 5. The 3-hour magnetic activity index, Kp, [Bartels, 1949] is broadly used because this index reflects the large-scale features of various levels of geomagnetic activity, which generally include electric potential drop across the polar caps, ionospheric conductivity magnitudes of both types, Hall and Pedersen, and others.

For control of simulation results and comparison with the observations, we used SuperMAG polar plots with ground magnetometers vectors, which represent equivalent ionospheric currents [Gjerloev, (2012), Waters, et al. (2015), and references therein].

To better understand the role of R2 currents and their effect on the entire ionosphere-magnetospheric current system, we performed several simulations with L-2015 model by choosing a simulation setup close to the selected real cases. We selected some of the cases to demonstrate the role of R2 currents in the magnetospheric substorm development.

We also compared the observations with the result of the simulation. First, we considered a moderate substorm on April 6, 2010 around 21:10 UT. The AU and negative AL indices are shown in the Figure 1, upper panel, and the components of the interplanetary magnetic field with steady negative Bz are shown in the lower panel. The pink shade indicates a time-zone of interest around 21:10 UT, though there is a time delay between certain IMF parameters and AE indices they produce.

Figure 2 shows the reconstructed electric field potential (a) and field-aligned current density (b) derived from the AMPERE data products for April, 06, 2010, 21:10 UT, and SuperMAG polar plots (c) with ground magnetometers vectors, which represent the equivalent ionospheric currents for the Northern (left) and Southern (right) hemispheres during the same period. The southern hemisphere is shown as a mirror image. For all AMPERE, SuperMAG and L-2015 simulation polar plots, the direction toward the Sun (12 MLT) is above each plot, and toward dawn (06 MLT) is on the right.

Equivalent ionospheric currents should not be mixed with real ionospheric currents. Ground magnetometers register magnetic variations, which are produced by two major currents systems: field-aligned currents and ionospheric currents. In the ground-based magnetometers data, we cannot separate these two effects. Therefore, for convenience, the observations could be interpreted as a result of flow of an imaginary ionospheric current system, with zero field-aligned currents. These equivalent ionospheric currents are defined as the divergence-free ionospheric current distribution, which produce the same magnetic field below the ionosphere as the original currents consisting of ionospheric and field-aligned currents [e.g., Fukushima, 1976; Kamide et al., 1981; Matsushita and Xu, 1982; Lyatsky and Maltsev, 1983; Amm and Viljanen, 1999; Weygand et al., 2012, and references therein]. These divergence-free equivalent ionospheric

currents are very convenient way to represent the spatial distribution of geomagnetic disturbances under the ionosphere, and our model allows this distribution to be calculated.

From the AMPERE images, Figure 2 (b), the R1 currents are visibly localized around 17°-18° of colatitude, while the location of weak R2 currents is around 26°. However, the same time, the SuperMAG images Figure 2 (c) show strong equivalent ionospheric currents reaching 30° colatitude of the auroral zone. Therefore, we made simulations for several different locations of R2 currents up to 30° colatitude.

For the first simulation we used the parameters of the event described above. The R1 currents location is set for 18° of colatitude, the R2 currents are on 26°. The total ionospheric conductivity is defined by two major factors: solar illumination and auroral precipitation [Lyatskaya et al. 2015 and references therein], which parameters are typical for KP = 4, e.g. the maxima of Pedersen and Hall conductivities are respectively 10.0 S and 18.0 S (after Hardy et al. [1987]). The electric field potential drop for the boundary conditions was taken from the AMPERE product (MIX ionospheric solver); it changes from -30 kV at the eastern boundary of the polar cap (18 MLT) to +42 kV at the western boundary (06 MLT). It should be noted that only potential drop is taken from MIX ionospheric solver, and the total potential distribution in the auroral zones was derived from the solution of the 3-D continuity equation for the currents in both ionospheres with Hardy model of ionospheric conductivity, as described in [Lyatskaya et al. 2015].

Figure 3 shows the electric field potential simulated with L-2015 for given boundary conditions and ionospheric conductivities in two hemispheres for the described case configuration. The calculated potential distribution is close to the results of the MIX model in the AMPERE products. Figure 4 shows the simulated equivalent ionospheric currents, for the

Northern (left) and Southern (right) hemispheres for the above case. The results of the simulation are as follows: the AU index is 929 and 895 nT for the northern and southern ionospheres; the AL index is -963 and -926 nT respectively. The magnitude of the indices is very close to the observational data (Figure 1 b), where we can see that the AU index in this time frame fluctuates between 800 and 1000 nT, and the AL index fluctuates between -600 and -800 nT.

For this model setup, the simulated electric field potential distribution (Figure 3) is very close to the AMPERE potential distribution shown on Fig. 2 a, but the equivalent currents maps Fig. 4 (bottom) differ significantly from Figure 2 (c): the SuperMAG plot shows a strong equivalent ionospheric current on the night side, while the simulated equivalent ionospheric currents decrease significantly from dawn side toward the night side. The strongest simulated westward electrojet current is in the day-to-dawn sector, with the strongest simulated eastward electrojet current being in the day-to-dusk region.

The obvious explanation for the reduction in ionospheric currents on the night side is that these currents flow across the auroral zone rather than along it. The highly conductive auroral zone of the ionosphere provides a robust connection between the R1 and R2 currents. To better understand this effect, the following simulation was performed for the same set of parameters except that the R2 current location was set to 28^{o} colatitude. The AU indices for this simulation are 744 and 714 nT for Northern and Southern hemispheres respectively, and the AL indices are -769 and -737 nT. Increasing the distance between the location of R1 and R2 currents results in a widening of the region of the equivalent ionospheric currents and a decrease in their magnitude. Further displacement of R2 currents to a lower colatitude, e.g. 30^{o} (Figure 5), leads to an even greater decrease in the magnitudes of the equivalent ionospheric currents, as well as in the AL and AU indices. In this case, the AU reduces to 610 and 583 nT for the Northern and Southern

ionospheres respectively; AL index changes to -626 and -598 nT for the same hemispheres. Moving R2 even further away from the R1 currents results in further reducing the magnitude of the equivalent ionospheric currents. However, the ionosphere still provides a connection between the R1 and R2 currents, and the ionospheric currents in the night sector will never reach the magnitude of SuperMAG data.

There is one more scenario which produces a westward auroral electrojet in the model through the night side to bring it closer to the SuperMAG data. This is the set of parameters, for which R2 currents are absent or small in magnitude, as well their shielding effect. This scenario is supported by AMPERE data, because the R2 currents around the period of interest are low in magnitude. The absence of intense R2 current means that their shielding effect is weak. In terms of auroral electrodynamics, the shielding effect on inner boundary of the plasma sheet determines the penetration of the electric field from the auroral zone to the lower latitude. In the context of inner magnetosphere models, the shielding effect from R2 currents was studied in numerical simulation by Jaggi and Wolf [1973] and analytically estimated by Maltsev [1974]. It is also routinely reproduced in ring current simulations. It has been shown with CRCM simulations of the ring current dynamics (Fok et al., 2010), that the shielding becomes weaker in the case of dynamic magnetic field variations (see Figure 3 from Fok et al., 2010). The April 6, 2010 event is characterized by intense and continuous auroral activity, so-called HILDAA events (Tsurutani et al., 2009, Hajra et al., 2013). The continuous auroral activity is likely causing magnetic field variations in the near-earth plasma sheet, and therefore weakens the shielding with a weakened R2 current system. AMPERE data confirms that the R2 currents are weak during the event of interest, despite strong auroral activity. It is important to note that the Dst_{min}

242 was equal -79 nT during the day, indicating the development of only a moderate geomagnetic
243 storm.
244 When R2 currents are weak, they cannot provide closure of the ionospheric currents. This
245 closure is provided by the auroral zone ionosphere, and under certain conditions by
246 interhemispheric currents. This mode was discussed and simulated in [Lyatskaya, et al. 2016];
247 the simulation showed appearance of a strong westward auroral electrojet in the night side
248 [Benkevich et al., 2000; Benkevich and Lyatsky, 2000; Lyatskaya et al., 2014, 2015, 2016].
249 However, the interhemispheric currents appear when there is a significant difference in
250 ionospheric conductivity between hemispheres. This difference could be substantial during
251 summer or winter season but not during spring and fall, when the two hemispheres are
252 illuminated roughly equally, and the influence of interhemispheric currents in the above cases
253 could be excluded. Therefore, in the next simulation setup we study the closure of the
254 ionospheric currents without interhemispheric currents and without R2 currents.
255
256 For this simulation, we set the R1 current location and all other parameters of the simulation
257 in the same way as in the above cases excluding only the R2 currents. The simulation showed
258 that in absence of R2 currents, there is no closure for R1 and ionospheric currents through the
259 equatorward boundaries of the auroral zone, therefore this closure is provided by the night side
260 ionosphere. However, with the above parameters, the magnitude of the equivalent ionospheric
261 current on the night side was far from observations, e.g., the AU and AL indices for the Northern
262 and Southern ionospheres are respectively: 332, 307, -310, and -312 nT.
263 To reproduce the observed values for auroral indices, we increased the electric field
264 potential drop across the polar cap for the simulation, from +105 kV to -75 kV. The outcome of

265 the simulations is shown in the Figures 6 and 7. There are predictably stronger ionospheric
266 currents and a strong westward auroral electrojet in the night sector. The AU and AL indices for
267 the Northern and Southern ionospheres are respectively: 830, 767, -776, -779 nT. In the polar
268 plots, we can observe that the equivalent ionospheric currents are now flowing along the auroral
269 oval on the night side, because the closure through R2 currents is not available.
270 The comparison between all the above cases is shown in the Figure 7. We plotted the
271 simulated with L-2015 horizontal component of the magnetic field that would be measured on
272 the ground in various sectors of the magnetic local time (MLT) of the auroral zone for the cases
273 described above. The upper (lower) magnitude of horizontal magnetic component recorded along
274 the entire auroral oval represents the AU (AL) index. These indices (Davis and Sugiura, 1966,
275 Tomita et al. 2011) show the disturbance level recorded by magnetometers located in the auroral
276 zone; they are directly related to the magnitude of equivalent ionospheric currents and therefore
277 present a convenient and widely used form of describing the level of activity.
278
279 In the Figure 7, the positive magnetic field variation is caused by the eastward auroral
280 electrojet, and its maximum represents the AU index for each hemisphere for this particular time.
281 The negative magnetic field is caused by the westward auroral electrojet, and its minimum
282 represents the AL index. The multicolored curves show the results of the simulations made for
283 the cases with the R2 currents set to 26^{o} (red line), 28^{o} (blue), 30^{o} (green), and 32^{o} (cyan). The
284 solid black curve shows the simulation result for the case where R2 currents are absent in the
285 model, but all the other parameters are the same as above. The black dashed curve shows the
286 results for the run with the R2 currents absent and the increased potential drop over the polar cap
287 (see Figure 6 for the maps of equivalent currents). The bold lines show the magnetic field

288 variation for the Northern hemisphere, and the thin lines show the results for the Southern
289 hemisphere. As the simulation is made for the spring season, the difference between the
290 magnitudes resulting from interhemispheric currents is negligible.
291 Figure 7 gives an overview in which MLT sector one can find the greatest magnitude of
292 the ionospheric currents. We also compare the model results with SuperMAG data and auroral
293 indices. As one can see, the red and blue lines for runs with R2 currents provide a good fit for the
294 AL and AU indices with observations. However, there is no model setup with strong R2 currents
295 that produces a strong westward electrojet in the midnight sector as suggested by the SuperMAG
296 data (Figure 2). The model setup, which corresponds to the observations with a strong midnight
297 electrojet, is the run without R2 currents, shown in the Figure 7 by dashed lines. This is also
298 consistent with AMPERE data, where no R2 currents appear around the simulation time. We
299 note that to obtain a strong electrojet for the model run without R2 currents, the potential drop
300 has been increased from ~75 kV to ~ 170 kV. We suggest that this discrepancy is the result of
301 several factors, including unambiguity in MIX solver solution, the effects of potential drop along
302 auroral field line and imperfect conductivity model in L-2015 model.
303
304 To further investigate the effects of R2 system on the ionospheric currents closure, we
305 analyzed another case of a magnetospheric substorm that occurred on April 5, 2010. The
306 substorm of April 5, 2010 happened after arrival at ~ 08:25 UT of CME-driven shock that
307 compressed the magnetosphere, applied Bz=-15 nT and caused a development of the extreme
308 geomagnetic substorm near 9:30 UT (Connors et al., 2011). It is believed that an unusually large
309 depolarization observed at GOES s/c at this time could be related to the Galaxy 15 s/c anomaly
310 and shows an example of space weather conditions that may have induced a major operational

311 anomaly (Connors et al., 2011). Since L-2015 does not currently include the effects of the
312 substorm current wedge, we selected for the analysis an early expansion phase around 09:10 UT,
313 where the effects of substorm current wedge are supposedly not very strong. The AU and
314 negative AL indices (top) and interplanetary magnetic field components (bottom) are shown in
315 the Figure 8. We can see that the AU and AL indices reach their maximum magnitude between
316 2000 and 2500 nT around 09:30 UT, and fluctuate in the range 1000-1500 nT around 09:10 UT.
317 There is a strong and stable southward IMF Bz component, and a strong and fluctuating By IMF
318 component around 09:10 UT.
319 Figure 9 shows the suggested electric field potential derived from MIX ionospheric solver
320 (a), field-aligned current density (b) derived from AMPERE data for April 5, 2010, 9:10, and (c)
321 SuperMAG polar plots with ground magnetometers vectors for the Northern (left) and Southern
322 (right) hemispheres. The AMPERE data does not show substorm current wedge signatures
323 around this time. The R2 currents are weak in the Northern hemisphere, but present in the
324 Southern hemisphere.
325
326 We made a set of simulations with the same approach: the R1 current location is set for 20^{o}
327 of colatitude as follows from the AMPERE polar plots on Figure 9, the R2 location is set for 30^{o},
328 32^{o}, 34^{o}, and 36^{o}, and also some cases were considered with R2 currents absent from the
329 simulations. The ionospheric conductivity parameters related to typical auroral precipitations for
330 KP = 5, e.g. the maxima of Pedersen and Hall conductivities are 12.5 S and 25.9 S respectively.
331 The electric potential difference for the boundary conditions was taken from the AMPERE polar
332 plot; it changes from -110 kV at the western boundary of the polar cap to +61 kV at the eastern
333 boundary (Figure 9 a). The maximum and minimum of a potential has moved from 06 and 18

MLT to 03 and 15 MLT respectively (as in the AMPERE data, Figure 9 a) due to strong By component of the interplanetary magnetic field. The resulting potential calculated from L-2015 for 9:10 UT of April 5, 2010 is shown in the Figure 10. Similar to the first case, the AMPERE product (MIX solver) is only used to set up the boundary condition.

We made a set of simulations setting up the R2 currents at 30^o, 32^o, 34^o, as well as the set of simulations with the R2 absent. For the case where the R2 current system is set to 30^o, the AU and AL indices for the Northern and Southern ionospheres are respectively: 2619, 2554, -2911, and -2877 nT. For the case, where R2 currents system is set to 32^o, the AU and AL indices are: 2131, 2071, -2345, -2315 nT. For R2 set to 34^o, the indices are: 1765, 1708, -1899, -1871 nT. The results for the equivalent currents for the case where R2 currents system is set to 32^o are presented in the Figure 11. The results for the setup with the R2 absent are shown in the Figure 12. In this case, the westward electrojet in the midnight sector in strong in magnitude. For the same potential drop as in the previous cases, we obtained the AU and AL indices for the Northern and Southern ionospheres respectively: 1376, 1315, -1192, and -1189 nT, which is close to the indices observed around 09:10 UT. We also performed a simulation for the increased potential drop and the results are shown in the Figure 12. The potential difference increased up to 222 kV (from -79 to 143 kV) did not improve the agreement with the observed AU and AL indices, which are respectively 1789, 1709, -1549, and -1546 for the Northern and Southern ionospheres. The further increase in this difference also did not improve the comparison significantly.

To summarize the results of the Figures 11 and 12, we conclude that for the event of April 5, 2010 for the northern hemisphere, the SuperMAG observations agree better with the run

where R2 currents are absent. Indeed, the observed electrojet signatures are weak in the morning sector and strong in the post-midnight sector, as predicted in the Figure 12 (left panel). The result is also consistent with AMPERE observations in the northern hemisphere where the R2 currents are weak near 09:10 UT. For the southern hemisphere the situation is more complex. The AMPERE data shows a relatively strong R2 system, thus demonstrating a strong asymmetry between two hemispheres that the L-2015 model cannot predict. This is probably because the current version of the L-2015 model does not take into account all mechanisms that produce asymmetry between two hemispheres, for example the potential drop difference along the field line for the auroral zone, and the asymmetry due to IMF By. The SuperMAG data is scarce but there is a clear signature of an enhanced electrojet in the morning sector, which is consistent with the result of the run with R2 in the Figure 11 (right panel). We conclude therefore that the asymmetry observed in the electrojet magnitude between two hemispheres is explained by the asymmetry in the R2 distribution, and predicted by the L-2015 model, if the L-2015 results are analyzed for each hemisphere separately.

Figure 13 shows the simulated magnetic field that would be measured on the ground in various magnetic local time (MLT) sectors of the auroral zone for the runs described above. The multicolored curves show the result of the simulation made for the cases, where the location in colatitude of the R2 currents was set to 30^{o} (red line), 32^{o} (blue), and 34^{o} (green). The solid black curve shows the simulation result for the case, where R2 is absent from the model setup but all other parameters are the same as above. The black dotted curves show the cases where the R2 is absent and the electric potential drop over the polar cap is increased to 222 kV, and the black dashed curves show the results with an increased potential drop up to 273 keV. The observed AU/-AL is approximately 1000 nT (Figure 8), therefore we conclude that the run without R2

agrees better with the magnetometer observations in the northern hemisphere, where the stations for AU/AL indices are located. As noted above, the L-2015 model predicts that for the southern hemisphere, where the R2 system is present in the AMPERE data, the agreement would be better with the R2 setup, and would produce stronger AU/AL signatures. Currently, this is difficult to verify as no AU/AL index is available for the Southern hemisphere.

3. Discussion and Conclusion

Modern global coupled models of the Geospace show highly complex, self-consistent and interconnected interactions between field-aligned currents and their ionospheric closures. Because of the complexity, cause and effect relationships are sometimes hidden in a global self-consistent solution. In this study, we demonstrated how the simple model of ionospheric electrodynamics could help unravel some important aspects of the effect of R2 currents on the entire auroral oval.

Generating multiple simulations, we have selected a few for this demonstration. The effects of R2 currents on the auroral ionosphere are confirmed by multiple numerical experiments. The main results could be summarized as follows:

1. A strong R2 current provides a robust closure for ionospheric currents originating from R1 via the auroral zone ionosphere. Since the conductivity of the magnetic field lines is much higher than the ionospheric conductivity, the availability of the connection via R2 current can drastically change the parameters of the auroral zone: ionospheric and field-aligned currents, magnetic fields measured on the ground, and auroral indices. In the model, the larger magnitude westward auroral electrojet is found to be in the day-to-dawn sector, while the ionospheric and equivalent ionospheric currents on the night side have a much lower magnitude.

2. The location of R2 currents also affects the distribution of ionospheric and equivalent currents, as well as ground magnetic field measurements. As the distance between the current systems R1 and R2 increases, the magnitude of ionospheric currents decreases as the ionospheric currents propagate to larger regions at lower latitudes.

3. When R2 current cannot provide proper closure, the night side ionospheric currents increase in magnitude. Therefore, the R1 current is closed via ionosphere of the auroral oval night side. Ionospheric currents flow from dawn to dusk over the night-side ionosphere. The simulations show the appearance of the westward auroral electrojet in the night region of the auroral zone in case of absent R2 currents.

4. For the case of 21:10 UT of April 6, we found that to obtain the equivalent currents of the magnitude registered by ground magnetometers shown by SuperMAG, the potential drop over the polar cap in the model should be greater to that suggested by AMPERE products.

5. For the case of 09:10 UT of April 5, we found that for the northern hemisphere, the SuperMAG data shows strong currents in the area from dusk to midnight, which agrees well with the results for the model run without R2 current. For the southern hemisphere, SuperMAG data shows strong currents in the MLT ~06 h sector. This characteristic is reproduced by the run with R2 located at 32^{o} magnetic colatitude. AMPERE data are in agreement with the model results, showing a weak R2 system in northern hemisphere and a visible R2 system in southern hemisphere.

It should be noted that the substorm current wedge is not included in our model, and we have studied the characteristics of the auroral zone currents without considering the additional system of currents forming the substorm current wedge. AMPERE data does not show any

425 additional current systems adjacent to R1 currents that could be indicative of an intense substorm
426 current wedge for two considered events, therefore justifying our approach. We anticipate that
427 substorm current wedge could affect the results, and consider this effect in the future works.
428
429 We demonstrated that a part of the night side westward electrojet could only appear if R2
430 currents are weak or absent. Still, the magnitude of the equivalent ionospheric current on the
431 night side is less than observed, if the model uses the electric potential derived from the
432 AMPERE products. It suggests that either potential drop over the polar cap is greater than that
433 proposed by the AMPERE group, or some additional factors, such as substorm current wedge,
434 the potential drop along the field line, or errors in the specification of auroral conductivity as a
435 function of Kp index. The clarification of these uncertainties will be the subject of future work.
436

437 ## 4. Acknowledgements:

438 This study was accomplished as a part of the NSF Research on Grant # 1744925 with the
439 Division of Polar Programs, National Science Foundation. For N. Buzulukova, this work has
440 been partially supported by NASA grant 80NSSC19K0085.
441 For the Solar Wind data we gratefully acknowledge the OMNIWEB team and especially Dr.
442 Natalia Papitashvili, NASA Goddard Space Flight Center, Mail Code 672, Greenbelt, MD 20770
443 https://omniweb.sci.gsfc.nasa.gov/ow_min.html
444 For the ground magnetometer data we gratefully acknowledge: INTERMAGNET, Alan
445 Thomson; CARISMA, PI Ian Mann; CANMOS, Geomagnetism Unit of the Geological Survey
446 of Canada; The S-RAMP Database, PI K. Yumoto and Dr. K. Shiokawa; The SPIDR database;

AARI, PI Oleg Troshichev; The MACCS program, PI M. Engebretson; GIMA; MEASURE, UCLA IGPP and Florida Institute of Technology; SAMBA, PI Eftyhia Zesta; 210 Chain, PI K. Yumoto; SAMNET, PI Farideh Honary; IMAGE, PI Liisa Juusola; Finnish Meteorological Institute, PI Liisa Juusola; Sodankylä Geophysical Observatory, PI Tero Raita; UiT the Arctic University of Norway, Tromsø Geophysical Observatory, PI Magnar G. Johnsen; GFZ German Research Centre For Geosciences, PI Jürgen Matzka; Institute of Geophysics, Polish Academy of Sciences, PI Anne Neska and Jan Reda; Polar Geophysical Institute, PI Alexander Yahnin and Yarolav Sakharov; Geological Survey of Sweden, PI Gerhard Schwarz; Swedish Institute of Space Physics, PI Masatoshi Yamauchi; AUTUMN, PI Martin Connors; DTU Space, Thom Edwards and PI Anna Willer; South Pole and McMurdo Magnetometer, PI's Louis J. Lanzarotti and Alan T. Weatherwax; ICESTAR; RAPIDMAG; British Artarctic Survey; McMac, PI Dr. Peter Chi; BGS, PI Dr. Susan Macmillan; Pushkov Institute of Terrestrial Magnetism, Ionosphere and Radio Wave Propagation (IZMIRAN); MFGI, PI B. Heilig; Institute of Geophysics, Polish Academy of Sciences, PI Anne Neska and Jan Reda; University of L'Aquila, PI M. Vellante; BCMT, V. Lesur and A. Chambodut; Data obtained in cooperation with Geoscience Australia, PI Marina Costelloe; AALPIP, co-PIs Bob Clauer and Michael Hartinger; SuperMAG, PI Jesper W. Gjerloev; Data obtained in cooperation with the Australian Bureau of Meteorology, PI Richard Marshall. For the Polar Plots with field-aligned currents and we gratefully acknowledge the Active Magnetosphere and Planetary Electrodynamics Response Experiment (AMPERE) team and the AMPERE Science Center for providing the Iridium derived data products, PI Brian Anderson, Haje Korth, and Shin-ichi Ohtani. The L-2015 model results used for the preparation of the Figures 3-7,10-13 will be upload to the public repository Zenodo upon acceptance of the paper.

5. References

Anderson, B. J. et al. (2008a), Statistical Birkeland current distributions from magnetic field observations by the Iridium constellation, Annales Geophys., 26, 671-687, doi:10.5194/angeo-26-671-2008.

Anderson, B. J., H. Korth, C. L . Waters, D.L.Green,V.G.Merkin,R.J.Barnes, and L. P. Dyrud (2014), Development of large-scale Birkeland currents determined from the Active Magnetosphere and Planetary Electrodynamics Response Experiment, Geophys. Res. Lett., 41, 3017–3025, doi:10.1002/2014GL059941.

Akasofu, S.-I. (1964), The Development of The Auroral Substorm. Planet. Space Sci. vol. 12, issue 4, 273-282, doi: 10.1016/0032-0633(64)90151-5.

Amm, O., and A. Viljanen (1999), Ionospheric disturbance magnetic field continuation from the ground to the ionosphere using spherical elementary current systems, Earth Planets Space, 51, 431–440.

Anderson, B. J., S.-I. Ohtani, H. Korth, and A. Ukhorskiy (2005), Storm time dawn-dusk asymmetry of the large-scale Birkeland currents, J. Geophys. Res., 110, A12220, doi:10.1029/2005JA011246.

Anderson, B. J., Olson, C. N., Korth, H., Barnes, R. J., Waters, C. L., & Vines, S. K. (2018). Temporal and spatial development of global Birkeland currents. Journal of Geophysical Research: Space Physics,123, 4785–4808. https://doi.org/10.1029/2018JA025254

Bartels, J. (1949) - The standardized index Ks and the planetary index Kp, IATME Bulletin 12b, 97.

491 Benkevich, L., and W. Lyatsky (2000), Detached vortices in equivalent ionospheric currents
492 in the winter dayside ionosphere, Geophys. Res.Lett., 27(9), 1375–1378,
493 doi:10.1029/1999GL003711.
494 Benkevich, L., W. Lyatsky, and L. L. Cogger (2000), Field-aligned currents between
495 conjugate hemispheres, J. Geophys. Res., 105(A12), 27,727–27,737,
496 doi:10.1029/2000JA900095.
497 Buzulukova, N., M.-C. Fok, T. E. Moore, and D. M. Ober (2008), Generation of
498 plasmaspheric undulations, Geophys. Res. Lett.,35, L13105, doi:10.1029/2008GL034164.
499 Connors, M., C. T. Russell, and V. Angelopoulos (2011), Magnetic flux transfer in the 5
500 April 2010 Galaxy 15 substorm: An unprecedented observation, Ann. Geophys., 29, 619–622,
501 doi:10.5194/angeo−29−619−2011.
502 Davis, T. N., and M. Sugiura (1966), Auroral electrojet activity index AE and its universal
503 time variations, J. Geophys. Res., 71, 785–801.
504 Fok, M.−C., Buzulukova, N., Chen, S.−H., Valek, P. W., Goldstein, J., and McComas, D. J.
505 (2010), Simulation and TWINS observations of the 22 July 2009 storm, *J. Geophys. Res.*, 115,
506 A12231, doi:10.1029/2010JA015443.
507 Fukushima, N. (1976), Generalized theorem for no ground magnetic effect of vertical
508 currents connected with Pedersen currents in the uniform-conductivity ionosphere, Rep. Ionos.
509 Space Res. Japan, 30, 35–40.
510 Ganushkina, N. Y., Liemohn, M. W., & Dubyagin, S. (2018). Current systems in the Earth's
511 magnetosphere. Reviews of Geophysics, 56, 309–332. Doi:10.1002/2017RG000590
512 Gjerloev, J. (2012), The SuperMAG data processing technique, J. Geophys. Res., 117,
513 A09213, doi:10.1029/2012JA017683.

514 Hajra, R., Echer, E., Tsurutani, B. T., and Gonzalez, W. D.: Solar cycle dependence of
515 High-Intensity Long-Duration Continuous AE Activity (HILDAA) events, relativistic electron
516 predictors?, J. Geophys. Res., 118, 5626–5638, https://doi.org/10.1002/jgra.50530, 2013.
517 Iijima, T., and T. A. Potemra (1976), The amplitude distribution of field-aligned currents at
518 northern high latitudes observed by TRIAD, J. Geophys. Res., 81, 2165–2174,
519 doi:10.1029/JA081i013p02165.
520 Jaggi, R. K., and R. A. Wolf (1973), Self-consistent calculation of the motion of a sheet of
521 ions in the magnetosphere, J. Geophys. Res., 78, 16,2852–16,2866.
522 Hardy, D. A., M. S. Gussenhoven, R. Raistrick, and W. J. McNeil (1987), Statistical and
523 functional representations of the pattern of auroral energy flux and conductivity, J. Geophys.
524 Res., 92, 12,275–12,294, doi:10.1029/JA092iA11p12275.
525 Kamide, Y., A. D. Richmond, and S. Matsushita (1981), Estimation of ionospheric electric
526 fields, ionospheric currents, and field-aligned currents from ground magnetic records, J.
527 Geophys. Res., 86, 801–813, doi:10.1029/JA086iA02p00801.
528 Kepko, L., McPherron, R.L., Amm, O. et al. Space Sci Rev (2015) Substorm Current Wedge
529 Revisited. 190: 1. doi:10.1007/s11214-014-0124-9
530 Lyatskaya, S., W. Lyatsky, and G. V. Khazanov (2014), Effect of interhemispheric field-
531 aligned currents on the region 1 currents, Geophys. Res. Lett., 41, 3731-3737,
532 doi:10.1002/2014GL060413.
533 Lyatskaya, S., G. V. Khazanov, and E. Zesta (2015), Interhemispheric field-aligned currents:
534 Simulation results, J. Geophys. Res. Space Physics, 119, 5600-5612,
535 doi:10.1002/2013JA019558.

Lyatskaya, S., W. Lyatsky, and E. Zesta (2016), Effect of interhemispheric currents on equivalent ionospheric currents in two hemispheres: Simulation results, J. Geophys. Res. Space Physics, 121, doi:10.1002/2015JA021167.

Lyatsky, W., and Y. P. Maltsev (1983), Magnetosphere-Ionosphere Interaction, Nauka, Moscow.

Lyatsky, W. B., Y. P. Malsev, and S. V. Leontyev (1974), Three-dimensional current system of magnetic substorm, Planet. Space Sci., 22, 1231–1247.

Maltsev, Y. P. (1974), The effect of ionospheric conductivity on the convection system in the magnetosphere, Geomagn. Aeron., 4, 128.

Matsushita, S., and W.-Y. Xu (1982), Equivalent ionospheric current systems representing IMF sector effects on the polar geomagnetic field, Planet. Space Sci., 30(7), 641–656, doi:10.1016/0032-0633(82)90025-3.

Murphy, K. R., I. R. Mann, I. J. Rae, C. L. Waters, H. U. Frey, A. Kale, H. J. Singer, B. J. Anderson, and H. Korth (2013), The detailed spatial structure of field-aligned currents comprising the substorm current wedge, J. Geophys. Res. Space Physics, 118, 7714–7727, doi:10.1002/2013JA018979.

Ohtani, S., S. Wing, P. T. Newell, and T. Higuchi (2010), Locations of night−side precipitation boundaries relative to R2 and R1 currents, J. Geophys. Res., 115, A10233, doi:10.1029/2010JA015444

Papitashvili, V. O., F. Christiansen, and T. Neubert (2002), A new model of field-aligned currents derived from high-precision satellite magnetic field data, Geophys. Res. Lett., 29(14), 1683, doi:10.1029/2001GL014207.

Sazykin, S., R. A. Wolf, R. W. Spiro, T. I. Gombosi, D. L. De Zeeuw, and M. F. Thomsen, (2002), Interchange instability in the inner magnetosphere associated with geosynchronous particle flux decreases, Geophys. Res. Lett., 29(10), doi: vol. 29, issue 10, doi: 10.1029/2001GL014416, 2002

Toffoletto, F., Sazykin, S., Spiro, R. et al. Space Science Reviews (2003) 107: 175. https://doi.org/10.1023/A:1025532008047

Tomita, S., M. Nose, T. Iyemori, H. Toh, M. Takeda, J. Matzka, G. Bjornsson, T. Saemundsson, A. Janzhura, O. Troshichev, and G. Schwarz. Magnetic local time dependence of geomagnetic disturbances contributing to the AU and AL indices. doi:10.5194/angeo-29-673-2011

Tsurutani, B. T., Verkhoglyadova, O. P., Lakhina, G. S., and Yagitani, S. (2009), Properties of dayside outer zone chorus during HILDCAA events: Loss of energetic electrons, *J. Geophys. Res.*, 114, A03207, doi:10.1029/2008JA013353

Waters, C. L., J. W. Gjerloev, M. Dupont, and R. J. Barnes (2015), Global maps of ground magnetometer data, J. Geophys. Res. Space Physics, 120, doi:10.1002/2015JA021596

Weygand, J. M., O. Amm, V. Angelopoulos, S. E. Milan, A. Grocott, H. Gleisner, and C. Stolle (2012), Comparison between SuperDARN flow vectors and equivalent ionospheric currents from ground magnetometer arrays, J. Geophys. Res., 117, A05325, doi:10.1029/2011JA017407.

Weimer, D. R. (2001), Maps of ionospheric field-aligned currents as a function of the interplanetary magnetic field derived from Dynamics Explorer 2 data, J. Geophys. Res., 106, 12,889–12,902, doi:10.1029/2000JA000295.

Yu, Y., J. Cao, H. Fu, H. Lu, and Z. Yao (2017), The effects of bursty bulk flows on global-scale current systems, J. Geophys. Res. Space Physics, 122 , 6139–6149, doi:10.1002/2017JA024168.

Zheng, Y., A. T. Y. Lui, M.-C. Fok, B. J. Anderson, P. C. Brandt, T. J. Immel, and D. G. Mitchell (2006), Relationship between Region 2 field-aligned current and the ring current: Model results, J. Geophys. Res., 111, A11S06, doi:10.1029/2006JA011603.

6. Figures

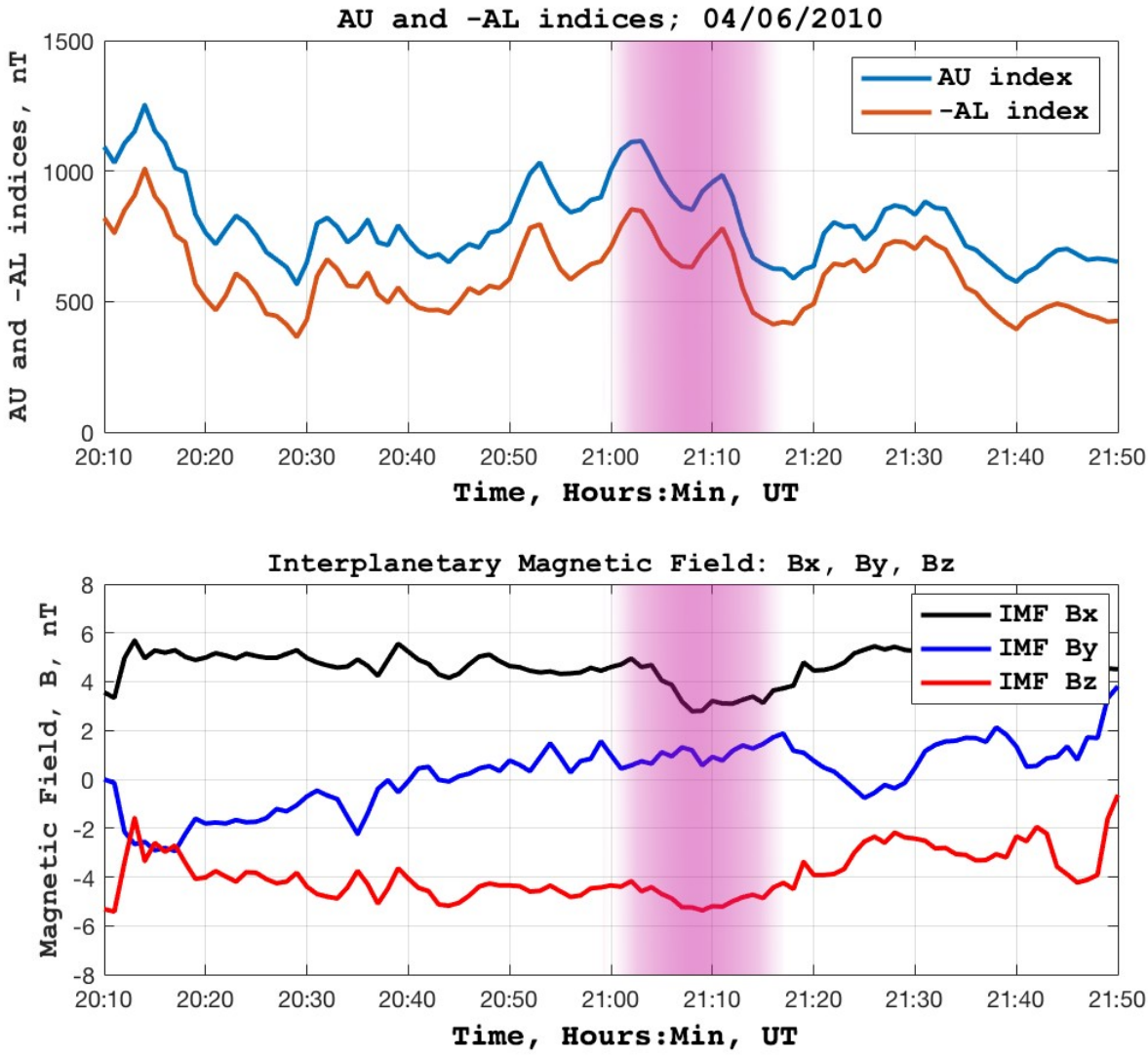

Figure 1. Top panel shows the AU and negative AL indices for April 06, 2010 from approximately 20:00 UT to 22:00 UT. The AU index is shown in blue and negative AL is shown in red. The lower panel shows the parameters of the interplanetary magnetic field (IMF): Bx (black), By (blue), and Bz (red). The pink shade indicates an interval of interest around 21:10 UT.

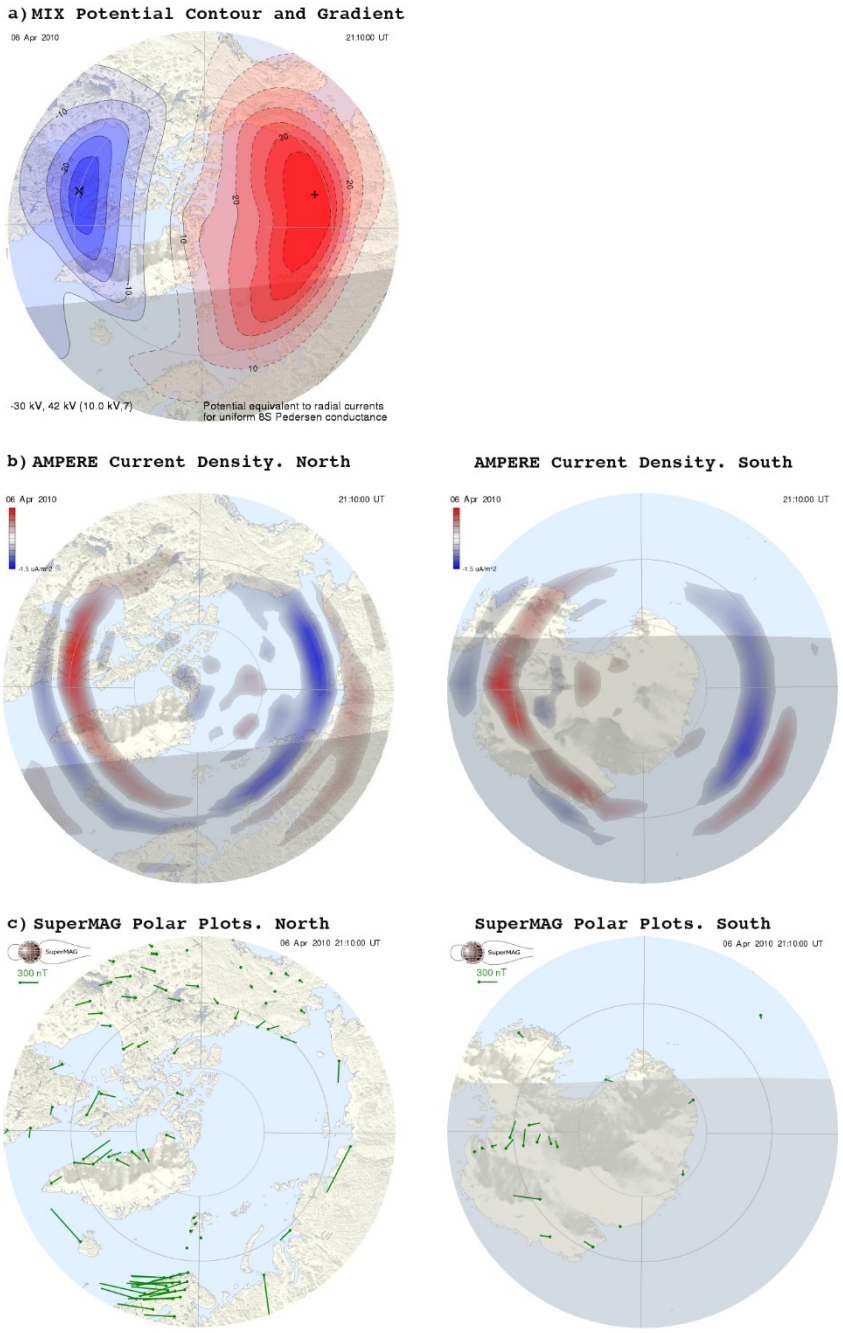

Figure 2. The electric potential (a) and field-aligned current density (b) from AMPERE data for April, 06, 2010, 21:10 UT. SuperMAG polar plots (c) with ground magnetometers vectors, which represent equivalent ionospheric currents for the northern (left) and southern (right) hemisphere for the same time. The southern hemisphere is shown as a mirrored image. The direction toward the Sun is above each plot, and towards dawn (06 MLT) is to the right. The enhanced electrojet region in the midnight sector is seen in panel (c) for the northern hemisphere.

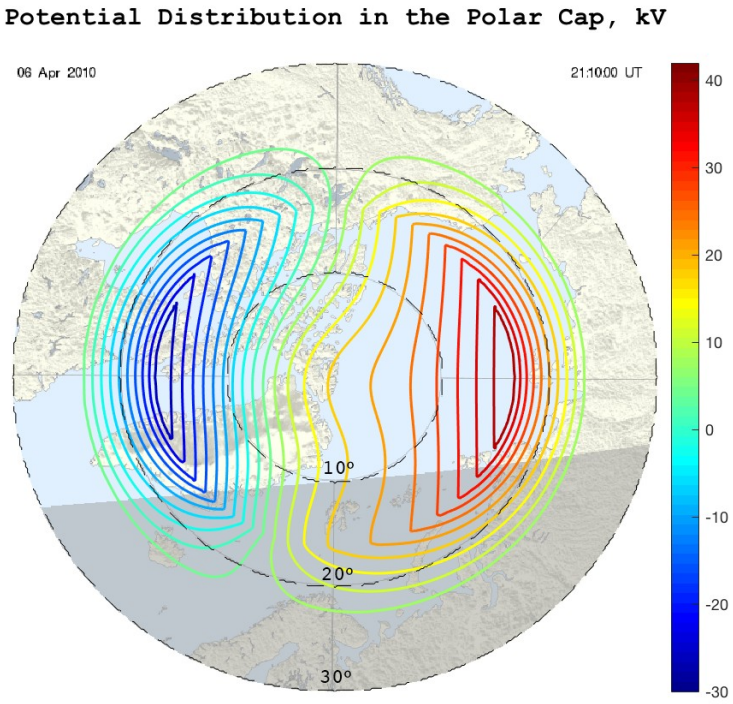

606
607

608 **Figure 3.** The electric potential simulated with the L-2015 model for April 06, 2010, 21:10 UT.
609 The parameters of the simulated event are: R1 current is located at 18° of colatitude, R2 current
610 is at 26°. The auroral precipitation parameters are typical for KP = 4. The electric potential
611 changes from -30 kV at the western boundary of the polar cap (18 MLT) to +42 kV at the eastern
612 boundary (06 MLT) as shown in the Figure 2 (a).
613

614

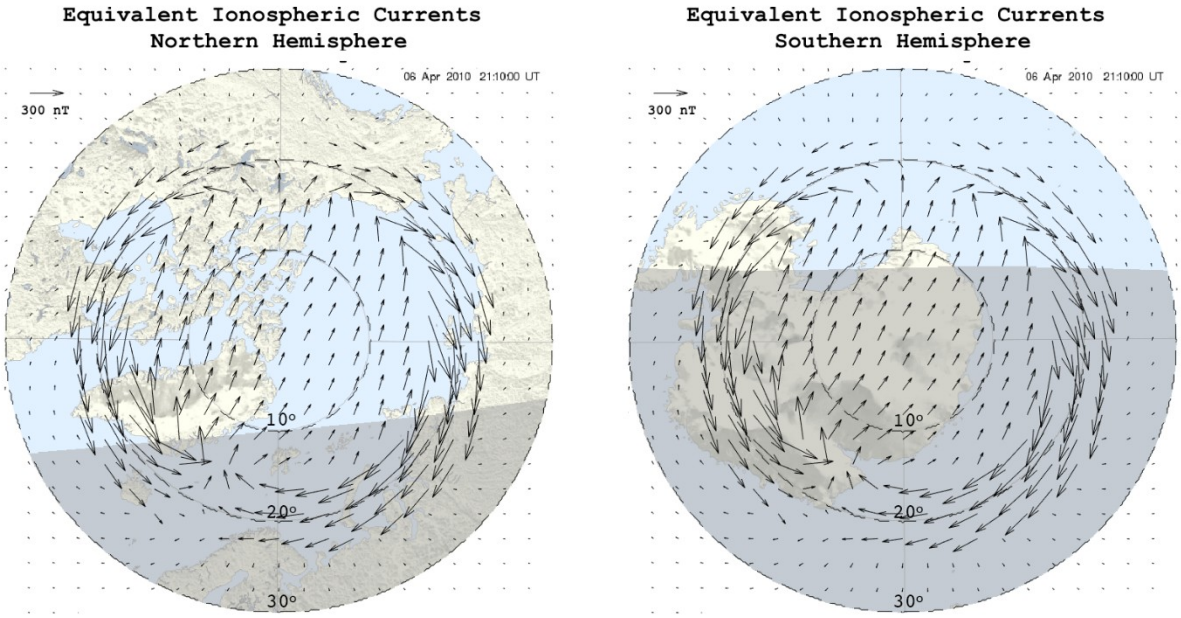

615
616 **Figure 4.** The simulated equivalent ionospheric currents, for the Northern (left) and Southern
617 (right) hemispheres for the case 1, where R1 currents are located at 18^{o} colatitude; R2 currents at
618 26^{o}; the ionospheric conductivity produced by geomagnetic activity is typical for KP=4, e.g. the
619 maxima of Pedersen and Hall conductivities are 10.0 S and 18.0 S respectively. The electric
620 potential changes from -30 kV at the western boundary of the polar cap (18 MLT) to +42 kV at
621 the eastern boundary (06 MLT) as taken from the Figure 2 (b). The Southern hemisphere is
622 shown as a mirrored image. Here and further, the direction to the Sun (12 MLT) is above each
623 image; the direction of dawn (06 MLT) is to the right. Note the absence of an electrojet near the
624 midnight sector in the distribution of equivalent currents.
625

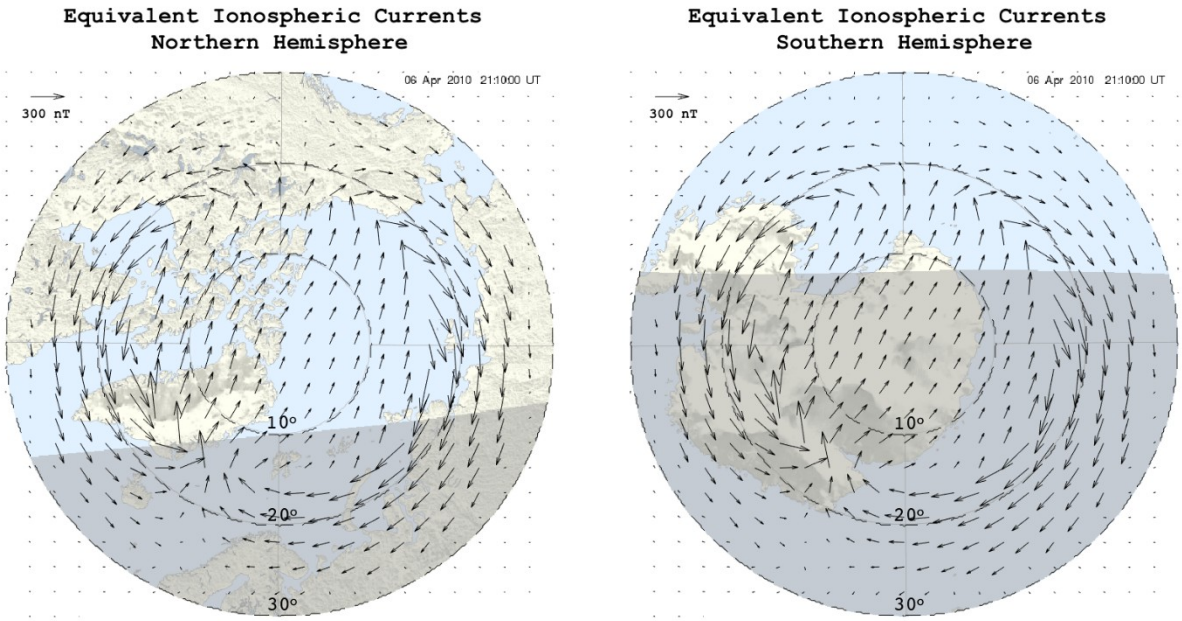

626
627 **Figure 5.** The simulated equivalent ionospheric currents, for the Northern (left) and Southern
628 (right) hemispheres for the case 2, where R1 currents are located at 18° colatitude; R2 currents at
629 30°. The electric potential changes from -30 kV at the western boundary of the polar cap (18
630 MLT) to +42 kV at the eastern boundary (06 MLT). Note the absence of the electrojet near the
631 midnight sector.
632

633

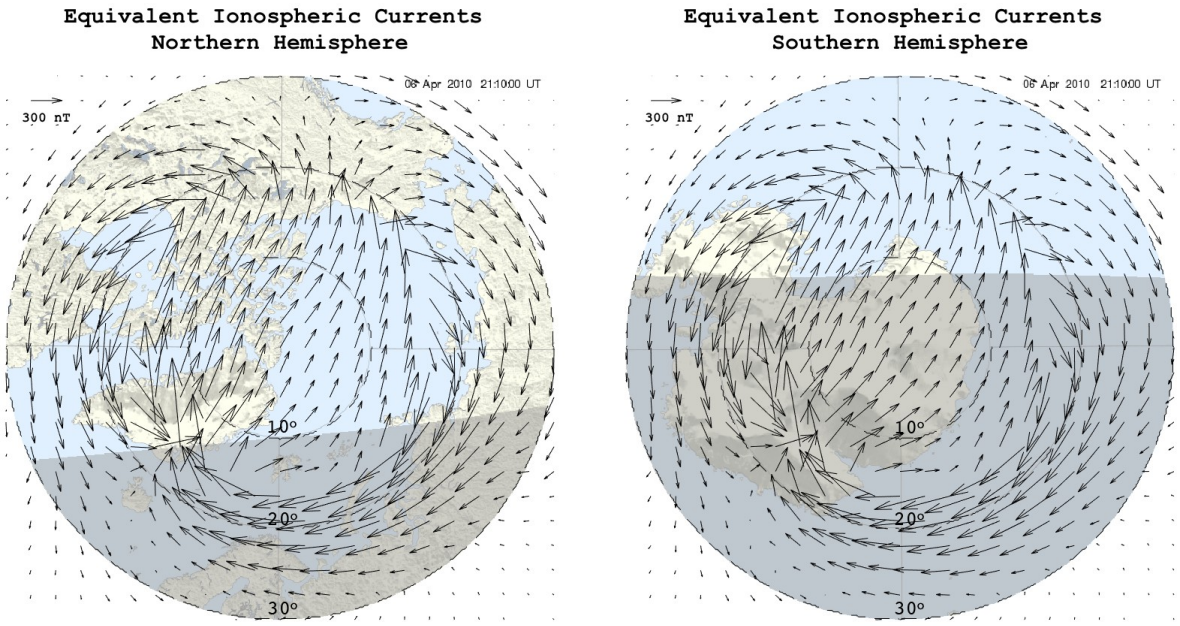

634

635 **Figure 6.** The simulated equivalent ionospheric currents, for the Northern (left) and Southern
636 (right) hemispheres for the case of negligible R2 currents and an increased electric potential drop
637 across the polar cap. The potential drop for the simulation is set to 180 kV, from -75 to +105 kV.
638 All other parameters of the simulation are the same. Note the appearance of the intense electrojet
639 near the midnight sector.

640

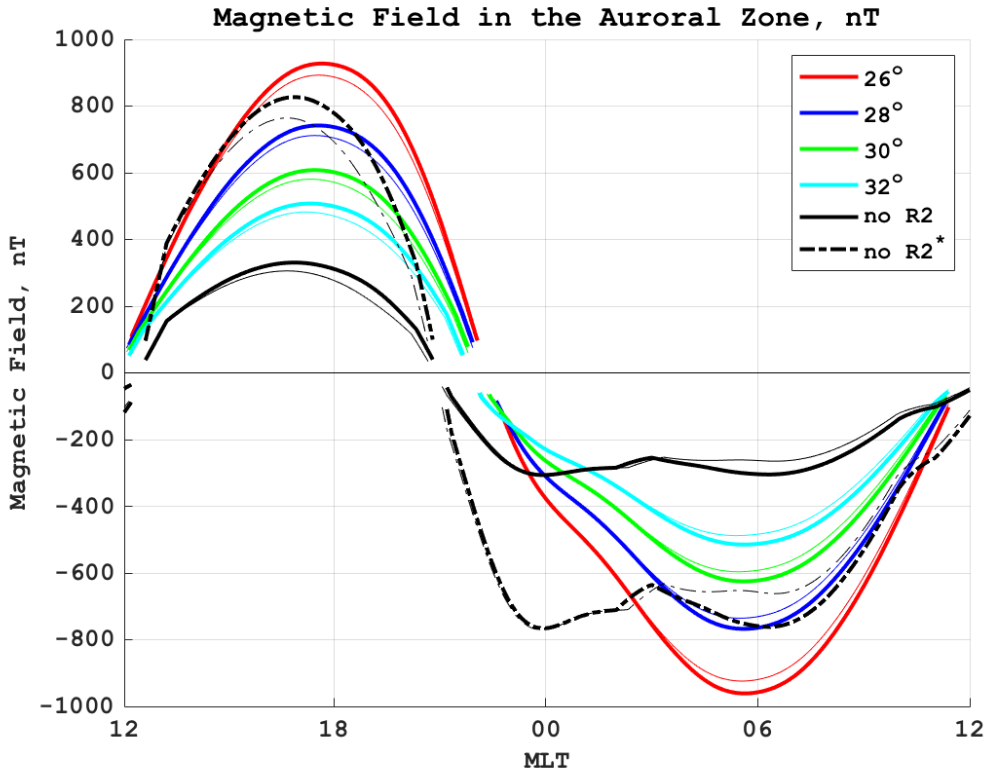

641

642 **Figure 7.** The simulated magnetic field that would be measured on the ground in various
643 magnetic local time (MLT) sectors in the area between R1 and R2 currents for the cases
644 described above. In case of absence of R2 currents, the auroral zone width is set to 12° below R1
645 current. The multicolored curves show the result of the simulation made for the cases with the
646 R2 currents set at 26° (red line), (Figure 4), 28° (blue), 30° (green), (Figure 5), and 32° (cyan).
647 The solid black curve shows the simulation result for the case where R2 is absent from the model
648 setup but all other parameters are the same as above. The black dashed curve shows the case with
649 the R2 is absent and electric potential drop over the polar cap is increased and set to 180 kV,
650 from -75 to +105 kV (Figure 6). The bold lines show the magnitude of the magnetic field in the
651 Northern hemisphere, thin lines show the results for the Southern hemisphere. As the simulation
652 is made for the spring season, the difference between the magnitudes for the two hemispheres is
653 negligible. The positive magnetic field is caused by eastward auroral electrojet; its maximum
654 represents AU index. The negative magnetic field is caused by westward auroral electrojet, its
655 minimum represents AL index for the time given. Note that currently measurements of AE
656 indices are available only for the Northern hemisphere.
657

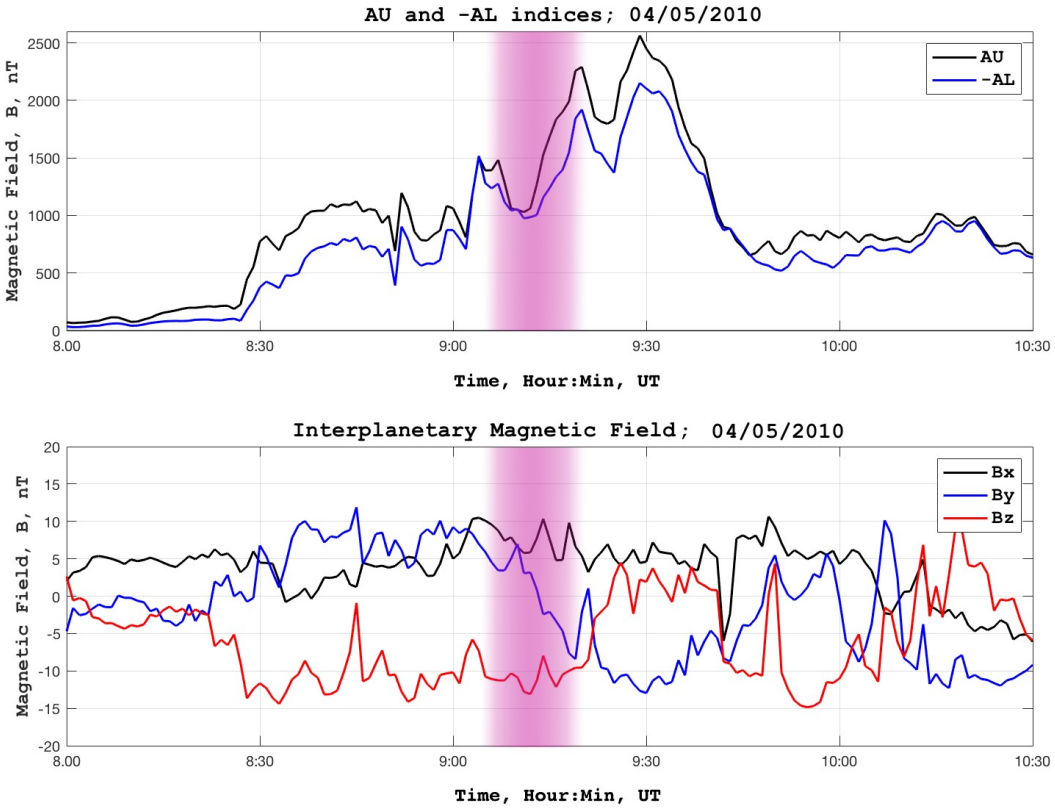

658
659

660 **Figure 8.** The top panel shows the AU and negative AL indices for the morning hours for April
661 05, 2010. The AU index is shown in black and negative AL is shown in blue. The lower panel
662 shows the parameters of the interplanetary magnetic field: Bx (black), By (blue), and Bz (red).
663

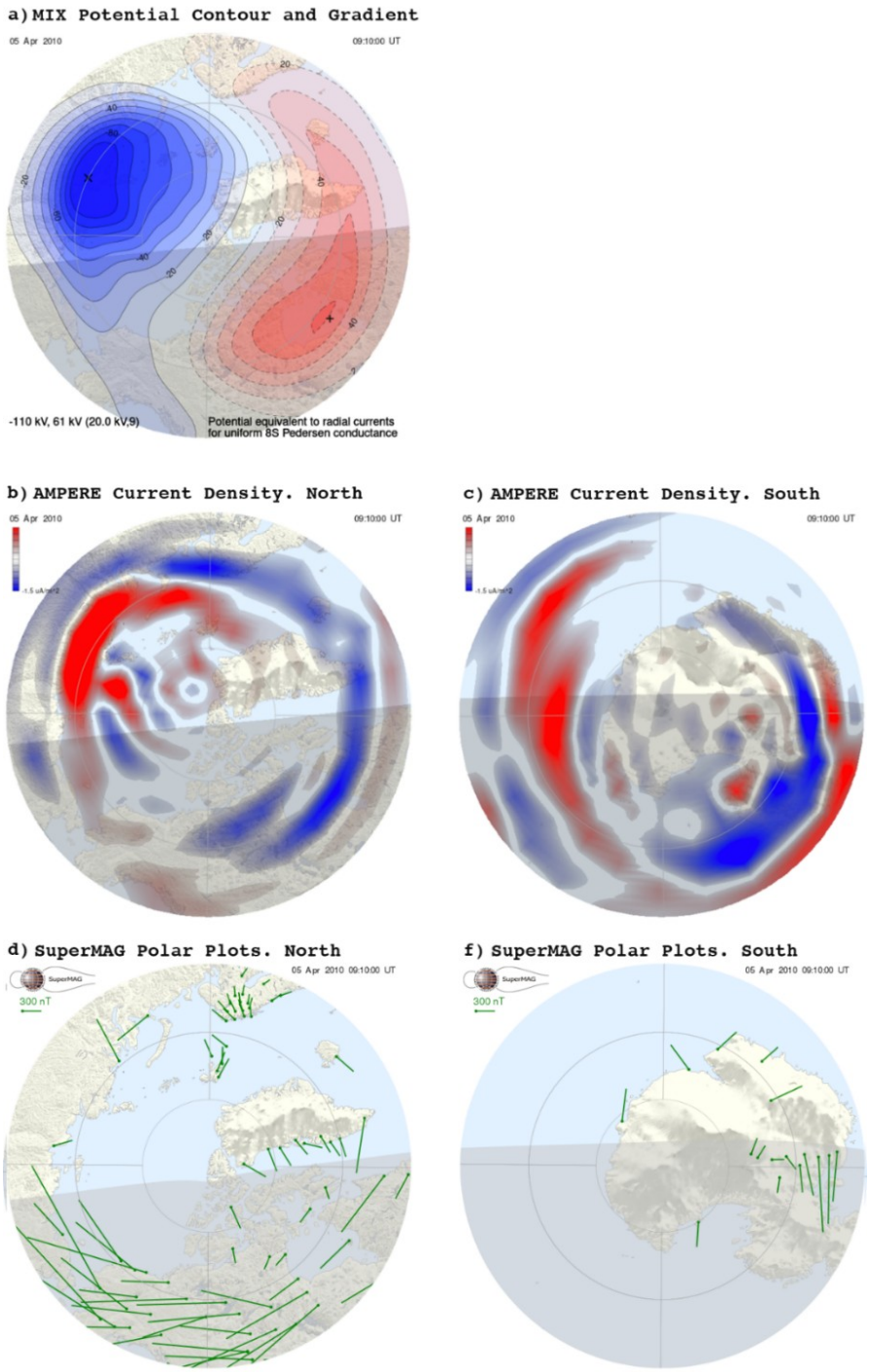

Figure 9. The electric field potential (a) and the field-aligned current density (b) derived from AMPERE data for April 05, 2010, 9:10 UT. SuperMAG polar plots (c) with ground magnetometers vectors, which represent equivalent ionospheric currents for the Northern (left) and Southern (right) hemisphere for the same time. The Southern hemisphere is shown as a mirrored image.

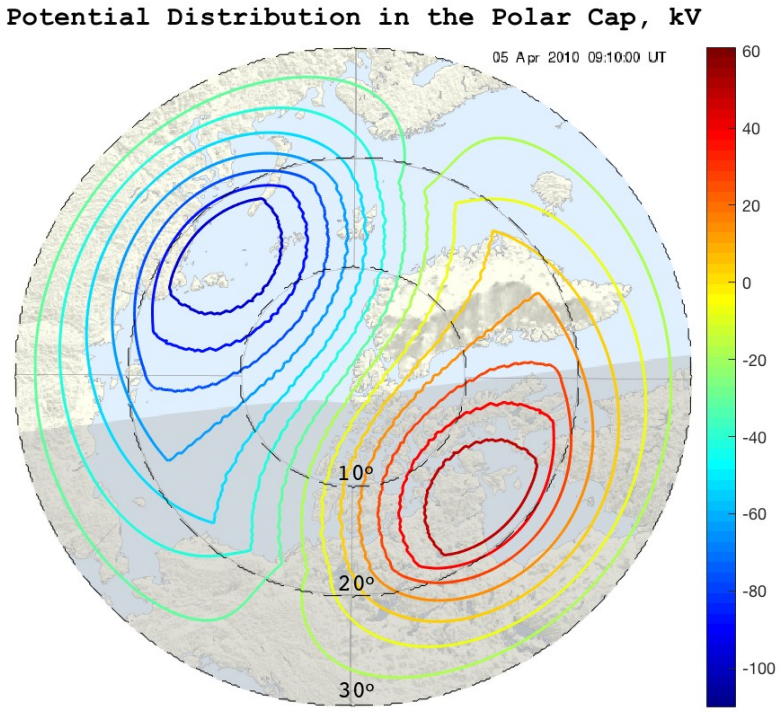

Figure 10. The simulated electric potential for April 5 2010, 9:10 UT with the L-2015 model. The parameters of the simulated case are: R1 current is located at 20° of colatitude, R2 current is at 30°. The auroral precipitation parameters are typical for KP = 5; the maxima of Pedersen and Hall conductivities are 12.5 S and 25.9 S respectively. The electric potential difference for the boundary conditions simulation changes from -110 kV at the western boundary of the polar cap to +61 kV at the eastern boundary, but the maximum and minimum of a potential shifted from 06 and 18 MLT to 03 and 15 MLT respectively due to By effect.

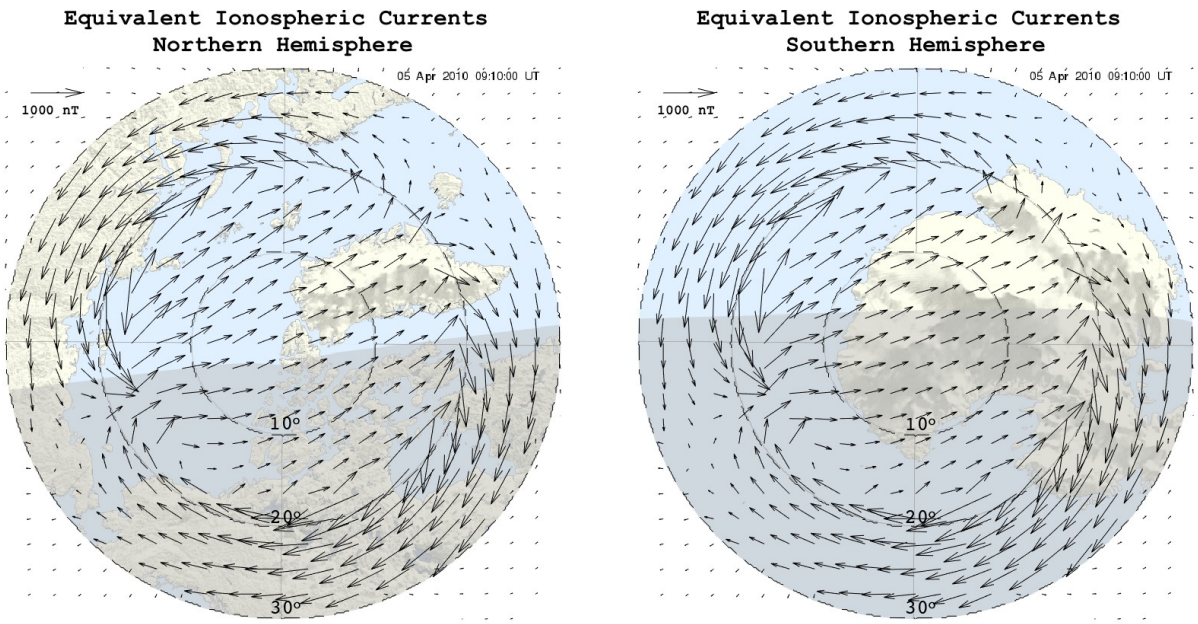

Figure 11. The simulated equivalent ionospheric currents, for the Northern (left) and Southern (right) hemispheres for the case, in which R1 currents are located at 20^{o} colatitude; R2 currents at 32^{o}; the ionospheric conductivity is typical for KP=5. The electric potential difference for the boundary conditions simulation changes from -110 kV at the western boundary of the polar cap to +61 kV at the eastern boundary as in Figure 10. Note that the reference vector for the images is set at 1000 nT.

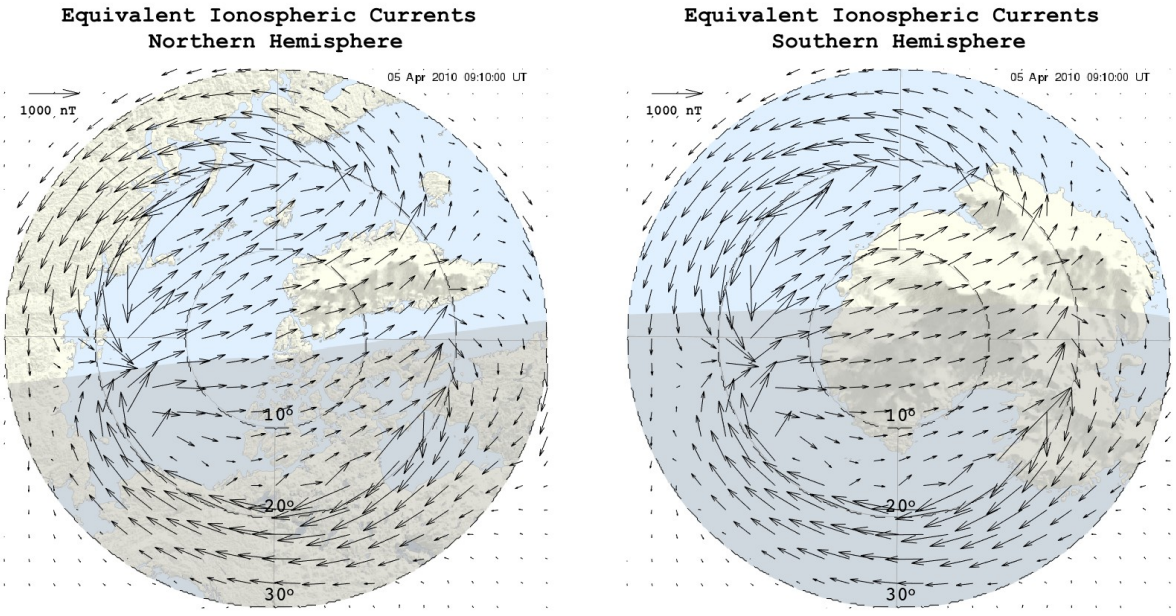

Figure 12. The simulated equivalent ionospheric currents, for the Northern (left) and Southern (right) hemispheres for the case of negligible R2 currents, while all other simulation parameters are the same as in Figure 11. R1 currents are located at 20° colatitude, the ionospheric conductivity is typical for KP=5. The electric field potential difference for the boundary conditions simulation changes from -110 kV at the western boundary of the polar cap to +61 kV at the eastern boundary.

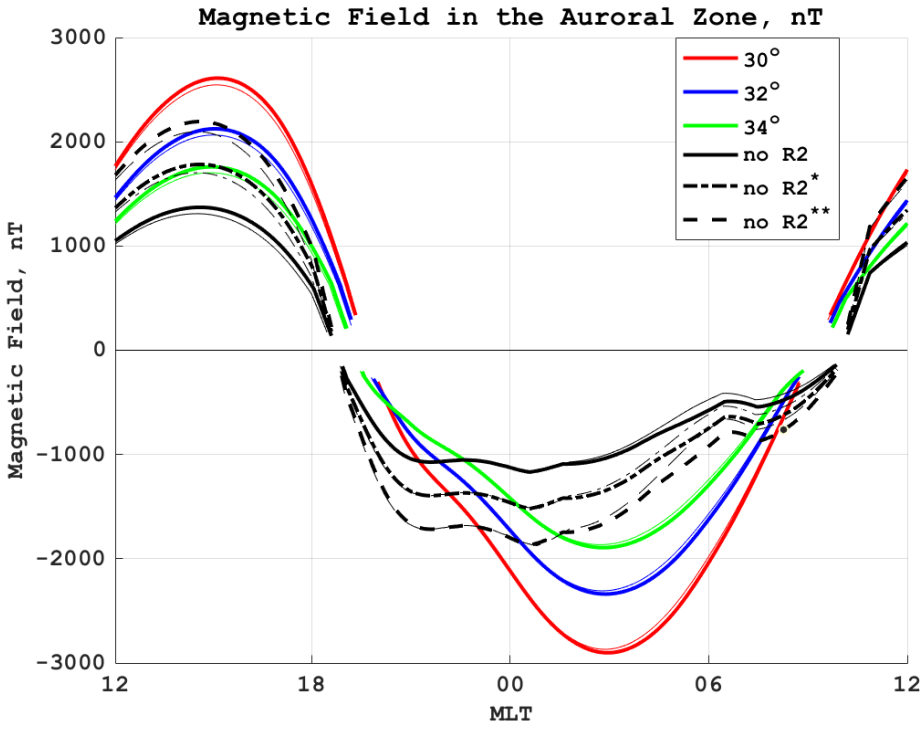

Figure 13. The simulated magnetic field which would be measured on the ground in different magnetic local time (MLT) sectors of the auroral zone for the case of April 05, 2010, 09:10 UT, for the model runs described above. The multicolored curves show the results of the simulation made for the cases with the R2 currents set to 30° (red line), 32° (blue), and 34° (green). The solid black curve shows the results for the case where R2 is absent from the model setup but all other parameters are the same as above. The black dash-dotted curve shows the results for the case with the R2 absent and the electric potential drop increased by 30% compared to the original case, up to 222 kV (from -143 to 79 kV). The black dashed curve shows the results for the run with the R2 absent and the potential drop increased by 60%, up to 273 kV (from -176 to +97 kV). The bold lines indicate the Northern hemisphere fields magnitude, with thin lines for the Southern hemisphere. The positive magnetic field is caused by eastward auroral electrojet; its maximum represents AU index for each hemisphere for the given time. The negative magnetic field is caused by westward auroral electrojet; its minimum represents AL index. The observed values for AU/-AL of ~1000 nT near 09:10 UT for the northern hemisphere agree well with the run without R2 currents.